International Journal of Rock Mechanics & Mining Sciences 86 (2016) 269–281

Contents lists available at ScienceDirect

International Journal of Rock Mechanics & Mining Sciences

journal homepage: www.elsevier.com/locate/ijrmms

Deformation forecasting and stability analysis of large-scale underground powerhouse caverns from microseismic monitoring

Feng Dai [a], Biao Li [a], Nuwen Xu [a,*], Yilin Fan [b], Chuanqing Zhang [c]

[a] State Key Laboratory of Hydraulics and Mountain River Engineering, College of Water Resource and Hydropower, Sichuan University, Chengdu, Sichuan, PR China

[b] China Three Gorges Corporation, Beijing, PR China

[c] State Key Laboratory of Geomechanics and Geotechnical Engineering, Institute of Rock and Soil Mechanics, Chinese Academy of Sciences, Wuhan, Hubei, PR China

ARTICLE INFO

Article history:
Received 14 May 2015
Received in revised form
22 March 2016
Accepted 4 May 2016
Available online 17 May 2016

Keywords:
Underground powerhouse caverns
Microseismic monitoring
Excavation
Stability analysis
Deformation forecasting

ABSTRACT

To assess the stability of the underground powerhouse caverns and analyse the failure mechanism of the surrounding rock mass at the Baihetan hydropower station in southwest China, a high-resolution microseismic (MS) monitoring system was implemented in the left-bank underground powerhouse caverns. Based on the temporal and spatial distribution of MS events, the correlation between MS activities and construction was established, and three damage regions for the surrounding rock mass during excavation were identified. MS clusters were found to occur most often in stress-concentration regions of the underground powerhouse caverns and to result from various factors, including excavation-induced unloading and geological structure activation. The seismic source parameters (i.e., moment magnitudes and (S-wave) to (P-wave) energy ratios, E_s/E_p) of the three MS clusters demonstrate the different failure modes and risks of the surrounding rock mass. The temporospatial evolution of the MS activities, apparent stress, and cumulative apparent volume in localized rock mass during the period of a typical large deformation were used to develop a comprehensive analytical method for forecasting the deformation of the surrounding rock mass. Thus, this comprehensive analytical method, which incorporates MS monitoring, conventional monitoring, geological survey and construction, is promising for identifying the damage zones and forecasting the macro-deformation of the surrounding rock mass in underground powerhouse caverns subjected to excavation.

1. Introduction

Numerous large-scale hydropower powerhouses have been or are being constructed in Southwest China, such as in Xiluodu, Dagangshan, Baihetan, Wudongde and Houziyan. Due to the restriction of the topographic and geological conditions and the construction types of hydraulic structures, it is difficult to arrange the ground powerhouses. Rather, these large-scale hydropower powerhouses are arranged as underground types. Large-scale underground caverns usually pass through various geological structures and surrounding rocks. Thus, the stability of underground caverns subjected to excavation plays a significant role in engineering safety. Methods for effectively forecasting and controlling the rock mass instability induced by the excavation of underground caverns have been critical in geotechnical engineering practices.

Considerable efforts have been made to assess the stability of underground caverns subjected to excavation, including numerical analysis, model testing, and in situ surveys and measurements. For instance, Zhu et al.[1] numerically investigated the stability of underground caverns in three representative hydropower stations and obtained best-fit formulae to predict the displacements of the sidewalls of the underground openings. Cai et al.[2] employed a coupled continuum discrete model to investigate the acoustic emissions (AE) activities during the excavation of underground caverns. The AE activities at the AE sensor locations matched well with the field monitoring results. The simulation results also provided the distribution of stresses and displacement in the rock mass for excavation design of the underground caverns. Alejano et al.[3] introduced the finite difference method as a means of predicting the subsidence due to flat and inclined coal seam mining. Dhawan et al.,[4] Wang et al.[5] and Wu et al.[6] conducted stability analyses on underground caverns using finite element methods, discrete element methods and discontinuous deformation analysis. Jing et al.[7] applied both continuum and discrete modelling approaches for the safety analysis of radioactive waste

* Corresponding author.
E-mail address: xunuwen@scu.edu.cn (N. Xu).

http://dx.doi.org/10.1016/j.ijrmms.2016.05.001
1365-1609/

repositories, coupling thermal, hydrological and mechanical (THM) processes. Zeng et al.[8] introduced underground models to reveal the failure shapes and mechanisms of underground caverns under complex geological conditions. Zhang et al.[9] studied the mechanical behaviour of stratified rock mass during excavation using physical model tests on assemblages of aluminium blocks consisting of weak portions of the model material interspaced with model joints. They also applied a discrete modelling code to study the effects of discontinuities on the behaviour of stratified rock masses. Li et al.[10] analysed the measured data on the displacement, deformation convergence, bolt load and EDZ (Herein, the EDZ was defined as excavation damaged zone of tunnels or underground caverns, including the near-field EDZ and the far-field EDZ. The near-field EDZ was likely to be induced by either a direct result of the excavation process or caused by stress redistribution and concentration around the tunnel. The far-field EDZ was usually dominated by the elastic effects caused by redistribution of the stress field) of surrounding rocks and predicted the behaviours of the loosened zones to optimize the support systems for a large-span cavern in the Baishan hydropower station in China. Hibino and Motojima[11] investigated the deformation of more than ten large-scale underground hydropower stations by field measurements. Yan et al.[12] analysed the transient in situ stress redistribution on EDZ of a deep-buried tunnel using field tests and numerical simulation. Recently, in situ measurement techniques (i.e., global positioning systems, multiple position extensometers and convergence meters) have been widely used in underground engineering. These monitoring results can sufficiently reflect the stress and surface deformation characteristics of the surrounding rock mass and provide validation for the numerical and model testing results. However, these techniques are ill-suited to monitoring inner micro-fractures, which usually occur prior to the macroscopic deformation or catastrophic failure of the surrounding rock mass. Therefore, it is crucial to effectively capture the micro-fractures to evaluate the excavation-induced risks of underground caverns.

MS monitoring, as a three-dimensional, real-time monitoring technique, can detect the micro-fracturing signals of rock and record them as seismograms. By analysing the waveforms, the time, spatial locations and source parameters of MS events can be obtained. Over the past two decades, the MS monitoring technique has been developed into an effective approach to assess the engineering hazards in many fields within rock slope engineering[13–15] and underground engineering, such as deep mining,[16–22] oil and gas storage,[23] tunnels[24–28] and electricity generation from hot dry rocks.[29] For instance, Xu et al.[14,15] analysed the temporospatial distribution of MS events, explored the dynamic failure process considering MS damage and assessed the stability of the left-bank slope in the Jinping first-stage hydropower station in Southwest China. Lesniak and Isakow[18] performed a hazard analysis based on the MS clusters of a coal mine and correlated the evaluated hazard function to the time of occurrence of high-energy tremors. Tang et al.[20] analysed the apparent stress and seismic deformation of a copper mine and predicted areal hazardous seismicity. Cai et al.[24,25] proposed a tensile model to estimate fracture sizes from MS measurements and quantify the rock damage of the AECL Mine-by Experiment test tunnel. Tang et al.,[26] Feng et al.[27] and Chen et al.[28] explored and summarized a rockburst mechanism based on the correlation between MS evolutional laws and rockbursts induced by the excavation of deep-buried tunnels. However, within these studies, the MS monitoring technique has rarely been employed in the stability analysis and deformation forecasting of large-scale underground powerhouse caverns, particularly during real-time excavation.

In this study, an MS monitoring system was implemented in the left-bank underground powerhouse caverns under construction at the Baihetan hydropower station, Southwest China. By analysing the temporospatial distribution of MS events, a correlation between MS activities and excavation schedule was established, and the potential failure regions were identified. Furthermore, the formation mechanism of MS events and associated seismic parameters involving moment magnitudes and *Es*/*E*p were investigated. Finally, a comprehensive method of forecasting the deformation of the surrounding rock mass based on MS activities, cumulative apparent volume and apparent stress was proposed.

2. Engineering background

2.1. Project description

The Baihetan hydropower station is currently under construction in the lower reaches of the Jinsha River between Sichuan and Yunnan Provinces, China. This project includes a 289-m-tall concrete double curvature arch dam, which controls a drainage area of more than 430,300 km^2. The two left- and right-bank underground main powerhouses contain eight units each, making this station the second largest in the world, with a total installed capacity of 16,000 MW. The left-bank large-scale underground powerhouse caverns are located in the upstream mountain of the dam, buried at a depth of 800–1050 m horizontally and 260–330 m vertically. These caverns mainly include pressure pipings, the main powerhouse, omnibus bar caves, the main transformer chamber, the draft tube bulkhead gate chamber, tailrace surge chambers and tailrace tunnels. The four main caverns (from upstream to downstream: main powerhouse, transformer chamber, draft tube bulkhead gate chamber and tailrace surge chamber) are arranged in parallel. The excavation dimensions of the main powerhouse are 438.0 m in length, 34.0 m in width, and 88.7 m in height. The designed excavation sizes of the main transformer chamber are 368.0 m in length, 21.0 m in width, and 39.50 m in height. The designed excavation dimensions of the draft tube bulkhead gate chamber are 374.5 m in length, 15.0 m in width, 94.0 m in height, while the four tailrace surge chambers have similar excavation dimensions of 44.5–48.0 m in diameter and 77.25–93.0 m in height. The thicknesses of the rock pillars between adjacent main caverns from upstream to downstream are 60.65 m, 40.95 m, and 46.95 m.[30] The layout of the left-bank large-scale underground powerhouse caverns is illustrated in Fig. 1. The underground powerhouse caverns were constructed using a conventional drill and blast method. The main powerhouse, transformer chamber and tailrace surge chambers were excavated using 10, 5 and 7 benches, respectively. The specific stratified excavation scheme of the underground group of caverns is shown in Fig. 2. Currently, four main underground caverns are being excavated at the first bench.

2.2. Formation lithologies

The left-bank slope of the hydropower station is steeply inclined toward the upstream side of the valley. Fig. 3 shows a typical formation cross-section of the left bank diversion power generation system along the 4# unit. The specific formation information is shown in Table 1. Overall, the diversion power generation system has a monoclinic formation, and the attitude of the basalt flow layer is with a strike of N42°–45°E, SE tendency, and a dip angle of 15°–20°. From upstream to downstream, the formations are in turn $P_2\beta_4$, $P_2\beta_3$, $P_2\beta_2$, and the lithologies include aphanitic basalt, oblique tholeiite, amygdaloidal basalt, breccia lava, tuff, and other materials. It is noteworthy that $P_2\beta_3^3$, $P_2\beta_3^2$ and $P_2\beta_4^1$ are mainly composed of the first, second, and third category of columnar jointed basalt, respectively. Furthermore, tuff

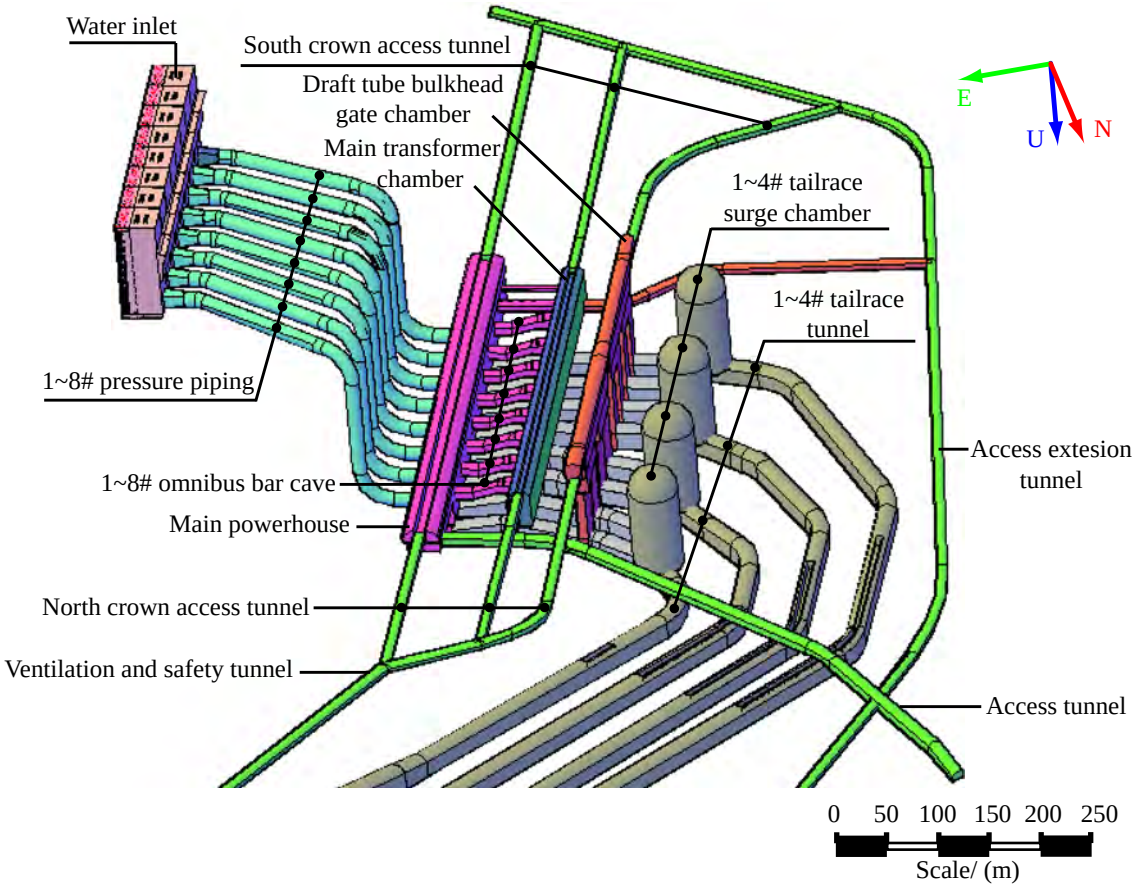

Fig. 1. Layout of the left-bank large-scale underground powerhouse caverns.

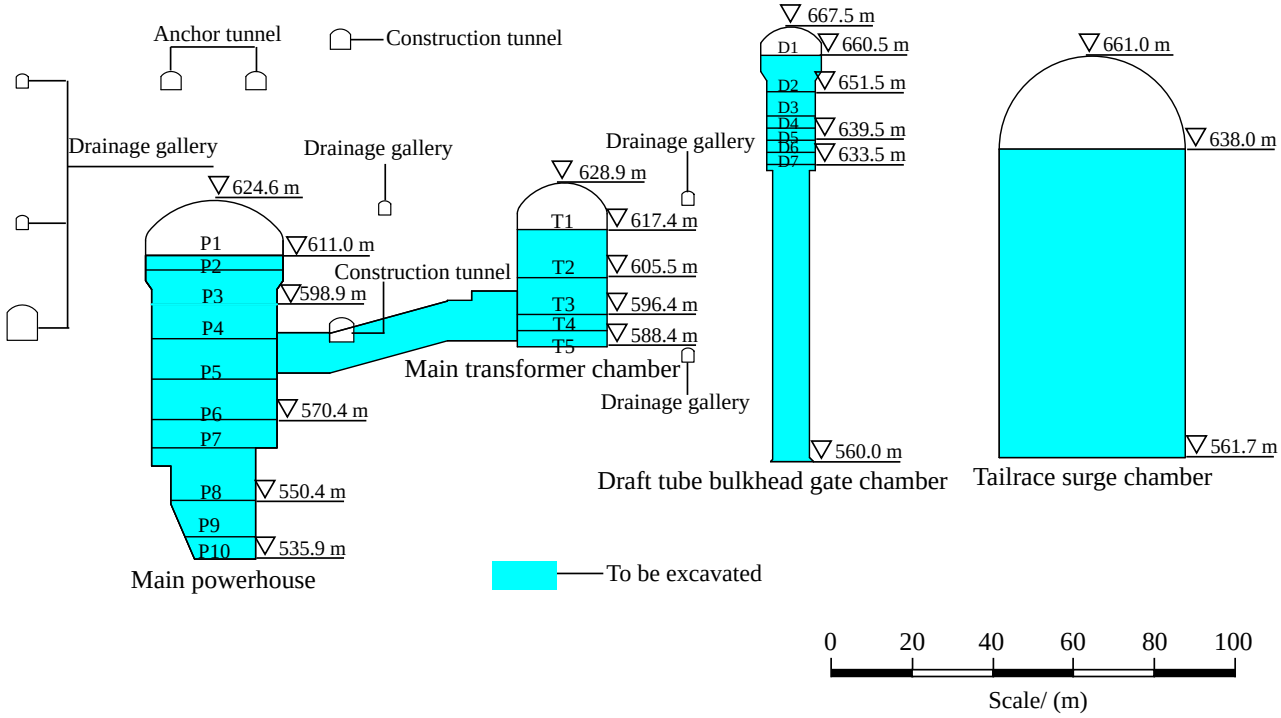

Fig. 2. Specific stratified excavation scheme of the underground powerhouse caverns.

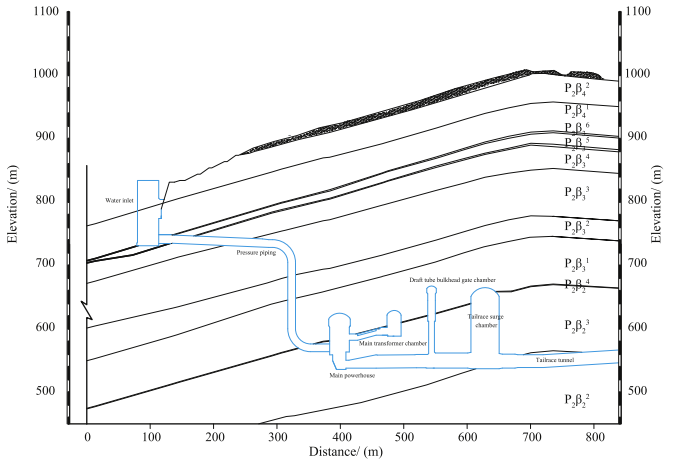

Fig. 3. A typical formation cross-section of the left bank diversion power generation system along the 4# unit.

breccia with a thickness of less than 1 m is mainly distributed along $P_2\beta_2^4$ and $P_2\beta_3^6$ on top of $P_2\beta_2$ and $P_2\beta_3$, in which the rock mass is weak and easily softened in water.[30]

2.3. Geological structures

The rock mass at the underground powerhouse caverns is relatively intact, and the surrounding rock masses are generally of intermediate quality. A stereographic projection of the main geological structures is shown in Fig. 4 to enable a thorough understanding of the main geological structures and the axis direction of the main underground caverns. Sixteen faults exist in this area, mainly hard structural planes and rock cuttings. The faults have several similar characteristics, such as N40°–70°W strikes, dip angles of more than 75° and translation property in major. Among the faults, f_{717}, f_{721}, f_{723} and f_{726} are large-scale, with lengths of 300–500 m and widths of 5–15 cm, while the others are relatively small-scale. The interlayer zone C2 aligns along the middle of the $P_2\beta_2^4$ tuff breccia with a width of 10–30 cm with a strike of N42°–45°E, SE tendency, and a dip angle of 14°–17°; this zone is mainly composed of mud cuttings and is easily softened in water. The seven exposed internal staggered zones are mainly hard structural planes and rock cuttings, most of which are small-scale, with lengths of 200–300 m and spacings of 10–30 m. Twenty-five long cracks are mainly hard structural planes with strikes of N40°–60°W and dip angles of 65°–85°, located between $P_2\beta_3^1$ and $P_2\beta_3^2$. The lengths of the long cracks are 50–100 m, and the spacings are generally 10–30 m. Three main crack groups develop with the following attitudes: (1) a strike of N30°–70°W, a tendency of SW and a dip angle of 65°–90°, (2) a strike of N20°–50°E, a tendency of SE and a dip angle of 10°–35° and (3) a strike of N50°–70°E, a tendency of SE and a dip angle of 50°–60°. The cracks are approximately 2–5 m long, with widths of less than 1 cm and spacings of 50–200 cm.[30]

2.4. In situ stress conditions

The in situ stress of the underground powerhouse caverns consists mainly of tectonic stress, with the horizontal stress exceeding the vertical stress. In general, the maximum principal stress and the second principal stress are nearly horizontal, and the minimum principal stress is almost vertical. The maximum principal stress is approximately 19–23 MPa, with a direction of N30°–50°W and a dip angle of 5°–13°, while the second principal stress is nearly 13–16 MPa. The minimum principal stress has a similar value (approximately 8.2–12.2 MPa) and direction to the self-gravity of the overlying rock mass.[30]

Affected by the complex arrangements of the numerous underground powerhouse caverns, adverse high in situ stress, various lithologies and geological structures, surrounding rock mass deformation and failure were frequently experienced during the excavation of the underground powerhouse caverns. Localized spalling of rock mass and weak rockbursts occurred as shown in Fig. 5. A real-time high-resolution MS monitoring system manufactured by Engineering Seismology Group (ESG), Canada, was thus installed in the left-bank underground powerhouse caverns to monitor the excavation-induced micro-cracking in the deep rock mass.

3. Excavation-induced MS activities

3.1. MS monitoring principle

An MS event is defined as a low-energy detectable acoustic or seismic signal associated with a sudden plastic deformation, such as the generation of new fractures or the propagation and movement of existing fractures.[31] Each MS signal captured and recorded as a seismogram contains a considerable amount of information, such as location, source radius, apparent stress, moment magnitude, and radiated energy, which can reflect the internal changes of the surrounding rock mass.[14] By analysing MS seismograms, seismic source information can be obtained. Once a sufficient number of MS events is recorded and processed, the variations in the strain or stress of the surrounding rock mass associated with microseismicity can be quantified.[14] Consequently, based on the dynamic evolution of MS events and source parameters, the potential failure or damage zones of the underground powerhouse caverns can be identified.

Micro-fractures can occur prior to the macroscopic deformation or failure of the rock mass, and MS events can thus be used as indicators of rock mass fracturing or damage when the rock mass

Table 1
Formation information of the left bank diversion power generation system.

Formations	Names	Main components
$P_2\beta_4^2$	The fourth group Emeishan basalt (the second subgroup)	Amygdaloidal basalt, breccia lava and aphanitic basalt
$P_2\beta_4^1$	The fourth group Emeishan basalt (the first subgroup)	The third category of columnar jointed basalt
$P_2\beta_3^6$	The third group Emeishan basalt (the sixth subgroup)	Tuff
$P_2\beta_3^5$	The third group Emeishan basalt (the fifth subgroup)	Amygdaloidal basalt and aphanitic basalt
$P_2\beta_3^4$	The third group Emeishan basalt (the fourth subgroup)	Amygdaloidal basalt, breccia lava and aphanitic basalt
$P_2\beta_3^3$	The third group Emeishan basalt (the third subgroup)	The first category of columnar jointed basalt
$P_2\beta_3^2$	The third group Emeishan basalts (the second subgroup)	The second category of columnar jointed basalt
$P_2\beta_3^1$	The third group Emeishan basalt (the first subgroup)	Amygdaloidal basalt, breccia lava and aphanitic basalt
$P_2\beta_2^4$	The second group Emeishan basalts (the fourth subgroup)	Tuff
$P_2\beta_2^3$	The second group Emeishan basalts (the third subgroup)	Aphanitic basalt and the second category of columnar jointed basalt
$P_2\beta_2^2$	The second group Emeishan basalt (the second subgroup)	Aphanitic basalt and the second category of columnar jointed basalt

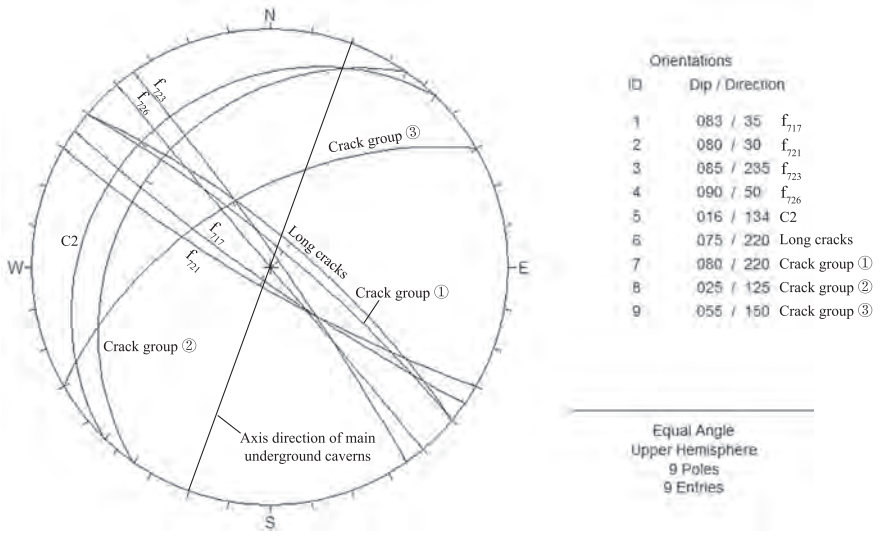

Fig. 4. Stereographic projection of the main geological structures in the underground powerhouse caverns.

Fig. 5. Photograph of rock mass spalling in the main powerhouse.

is approaching failure. The excavation-induced damage zones in the underground powerhouse caverns can then be identified and assessed. In particular, during the intensive excavation-induced unloading process of the deep caverns, MS activities can reveal the stress adjustment and redistribution within the rock mass. Additionally, several waveform parameters of MS events (i. e., peak amplitude, ring-down count, rise-time and event duration) facilitate further investigations of rock fracture mechanisms that result in macroscopic rock mass deformation or failure.[32] Therefore, the MS monitoring technique has been efficiently applied to analyse underground engineering risks.[21,27] To date, MS monitoring studies have mainly focused on four aspects: (1) counting the number of MS events and establishing a correlation between the MS rate, accumulated energy release and field construction; (2) locating the hypocentre of the MS events; (3) analysing full waveform data; and (4) identifying and revealing potential unstable regions and sliding surfaces of underground caverns from seismic data during the excavation period.[14]

3.2. Configuration of the MS monitoring system

The MS monitoring system mainly consists of a Hyperion digital signal processing system, a Paladin digital signal acquisition system, and six uniaxial accelerometer sensors. The network topology of the MS monitoring system is illustrated in Fig. 6. Six uniaxial accelerometer sensors with a flat frequency response from 50 Hz to 5 kHz ($\pm$ 3 dB) were deployed in boreholes drilled from the sidewalls of drainage tunnels in the underground powerhouse caverns. The MS signals were received by the uniaxial accelerometer sensors and transported to the Paladin digital signal acquisition system using copper twisted-pair cables. Through 24-bit analogue-to-digital conversion, the MS signals were transformed to digital signals in the Paladin digital signal acquisition system, which was connected to the Hyperion digital signal processing system by meshwire. The digital signals were then collected by the Hyperion digital signal processing system and automatically recorded as integral waveforms and spectra.[14]

Currently, four main caverns are being excavated at the first bench (Fig. 2). Prior to the formation of the high sidewalls, the crown areas of the underground powerhouse caverns in particular require investigation. Once the main monitoring area and the number of the sensors to be installed are determined, the sensors must be arranged properly for optimal MS locating and sufficient monitoring. Based on the critical monitoring area, arrangement density and installation feasibility of the sensors,[33] a thoroughly optimized sensor array was set up (Fig. 7). Six uniaxial accelerometer sensors were placed in the anchor branch tunnels located upstream and downstream of the main powerhouse, covering almost the whole crown area of the main powerhouse, the transformer chamber and the draft tube bulkhead gate chambers, and the upstream crown area of the tailrace surge chambers. Next, tap tests were conducted close to the sensors to verify the reliability of the sensors. Meanwhile, to determine the (P-wave) velocity and the location error of the MS monitoring system, a joint investigation of seismic wave velocity tests and on-site blasting tests was carried out. Five artificial fixed-point blasting positions in the underground caverns were accurately measured using a total-station. According to the seismic wave velocity measurements, the wave velocity value of rock mass was approximately between 4500 m/s and 5500 m/s. Then eleven (P-wave) velocities (4500 m/s, 4600 m/s, 4700 m/s … 5500 m/s) were set in the MS monitoring system respectively to locate these blasting events. Compared with the real blasting locations, the mean location error of each wave velocity for locating the five blasting events can be acquired. The wave velocity with the least mean location error was set as the rock mass velocity, while the least mean location error was determined as the location error of the MS monitoring system. The final P- and (S-wave) velocities used for the MS system were calibrated as 5000 m/s and 2887 m/s, respectively. The average location error was less than 5 m, which indicated that the MS

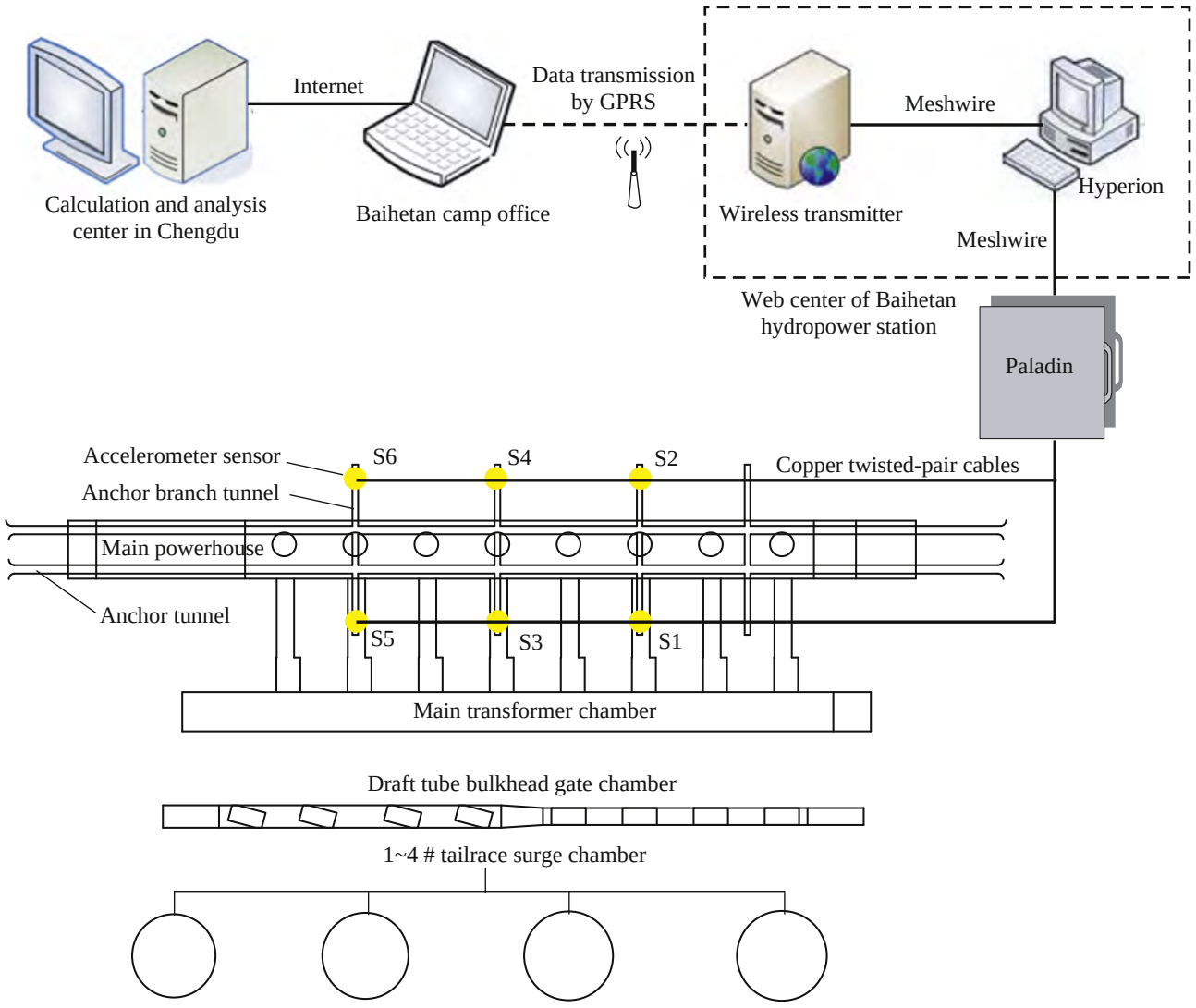

Fig. 6. Topological sketch of the microseismic monitoring network in the Baihetan hydropower station.

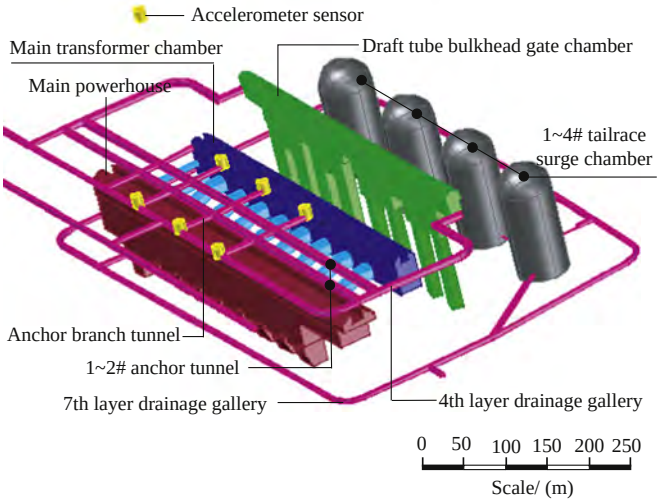

Fig. 7. Schematic of the accelerometer sensor array at the underground powerhouse caverns of the Baihetan hydropower station.

monitoring system had high positioning accuracy. The Paladin processing system was set up with a sampling frequency of 20 kHz. A triggering threshold was set by the ratio of the Short Time Average vs. Long Time Average algorithm (STA/LTA). To satisfy the location accuracy, at least four accelerometer sensors should be simultaneously triggered to record the waveform data.[28] The recorded waveforms can be processed either in manual or automatic mode to calculate the MS source parameters, including location, source radius, apparent stress, moment magnitude, and radiated energy. Moreover, the contours of various MS source parameters can be used to understand the mechanical behaviours of the deep rock mass. Typical waveforms for the recorded MS events are shown in Fig. 8.

3.3. Temporal distribution of microseismicity

The MS monitoring system began operation on October 10, 2014. In the real-time monitoring process, numerous signals including MS events, production blasts and other construction noises from different constructions and machineries were recorded. The continuous characteristics of microseismicity were highlighted in the underground powerhouse caverns. After filtering out the disturbing signals, 884 MS events were captured through December 15, 2014. Fig. 9 illustrates the temporal distribution of MS activities, MS cumulative energy and blasting activities. It can be observed that 0–58 MS events occurred each day, with approximately 13 MS events per day on average. During the excavation of underground powerhouse caverns,

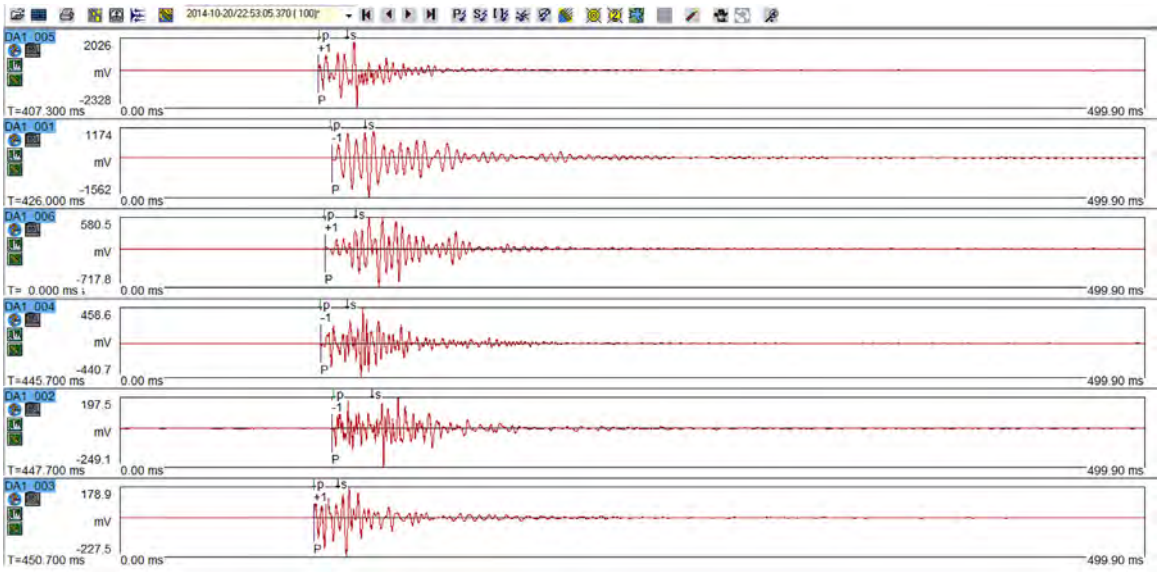

Fig. 8. Typical waveforms for the MS events recorded in the underground powerhouse caverns.

MS events occurred frequently between October 17–23 and November 11–18. The number of MS events per day was at least approximately 20. During these periods, the MS cumulative energy quickly increased (grey line in Fig. 9), and the number of blasting events (pink line in Fig. 9) indicated frequent excavating construction on site, which was in good agreement with the dynamic excavation. According to on-site observations and construction situations, the MS events were deduced to mainly result from the first bench excavation of the four main underground caverns. The mechanism of the microcracking extension induced by excavation is involved in two major phenomena: (1) excavation impact, including explosive loads and excavation-induced unloading, and (2) stress redistribution after excavation.[34] As is known, microcracking caused directly by explosive loads and excavation induced unloading is transient when the drilling and blasting method is adopted. Stress redistribution after excavation is another factor in microcracking. Relative to the direct excavation impact, stress redistribution after excavation has a stronger and longer influence on MS activities, particularly under high stress and in geological structure regions prone to stress concentration.

The MS events sharply increase up to a total of 58 on October 20, 2014. Considering the construction process, this abrupt increase in MS events was mainly induced by the excavation of the main powerhouse. An abnormal increase in MS events usually reflects intense stress change and stress redistribution of surrounding rock mass in the underground powerhouse caverns subject to excavation, which may directly result in large deformations or instable failures of the surrounding rock mass.[32,35] Further research on this abnormal increase in MS events will be reported in Section 4.1.

3.4. Spatial distribution of the microseismicity

Fig. 10(a) and (b) show the spatial distribution of MS events (spheres in Fig. 10(a) and (b)) in the underground powerhouse caverns recorded from October 10 to December 15, 2014. Different sphere colours represent different moment magnitudes, while different sizes represent different energy scales. It can be seen in Fig. 10(a) that most MS events were distributed around the crown of four main caverns, which were correlated with the first bench excavation of the caverns (see Fig. 2). Fig. 10(b) shows that MS event clusters mainly occurred in Zones I, II and III, where Zone I was located near the downstream spandrel between unit 4 and unit 5 of the main powerhouse, Zone II was located near the upstream spandrel between unit 6 and unit 7 of the main powerhouse, and Zone III was aligned along the crown above unit 7 and unit 8 of the main powerhouse to the crown of the transformer chamber. These three MS event clusters were the main damage zones and potential instable areas of the underground caverns during the monitoring period. Furthermore, Fig. 10(c) and (d) show

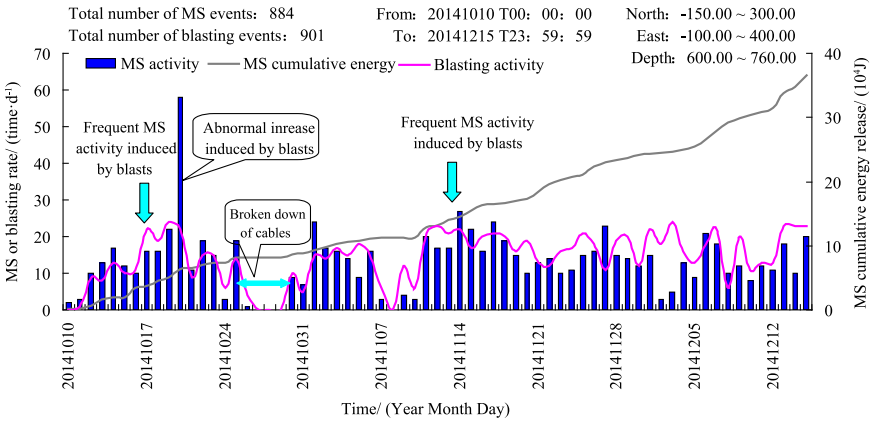

Fig. 9. Temporal distribution of MS activities, MS cumulative energy and blasting activities.

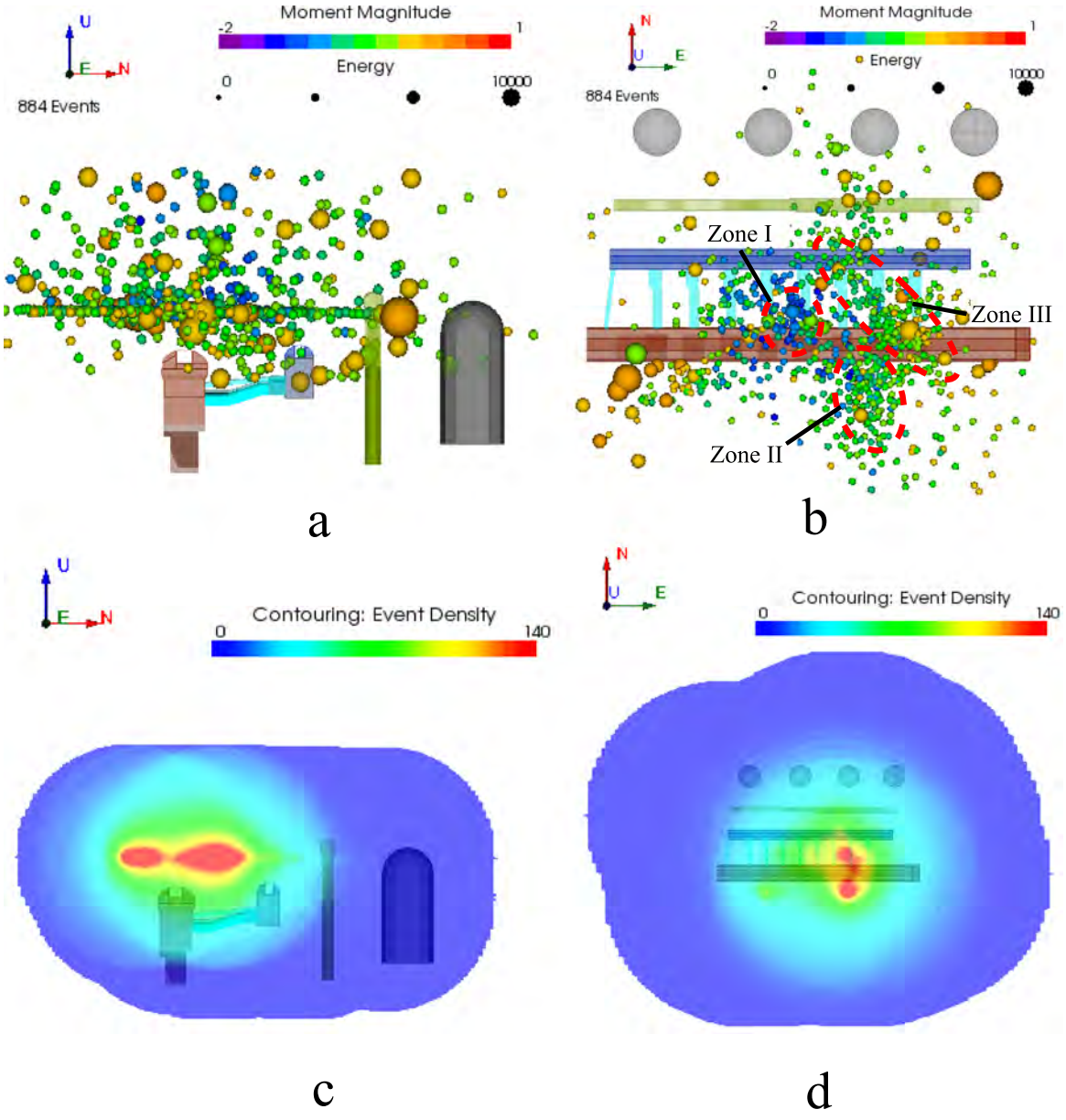

Fig. 10. Spatial distribution and density contour of MS events. (a) Front view and (b) top view of MS events and (c), (d) the density contours of MS events corresponding to (a) and (b), respectively.

the MS density contours of Fig. 10(a) and (b), respectively. According to the construction situations in Fig. 2, four large-scale cavern excavations were the main cause of this distinctive MS clustering phenomenon. In addition, excavation of the drainage tunnels and traffic tunnels also contributed to the occurrence of MS event clusters.

Rock mass damage was a phenomenon of state instability essentially driven by the radiated energy of MS events.[15] The values of radiated energy represented the degrees of rock mass damage; thus, the high energy-release zones should receive more attention due to the severity of the rock mass damage. Fig. 11(a) shows the energy density of MS events and demonstrates that the main MS energy release areas were Zones II and III (see in Fig. 10(b)). In Fig. 10(b), myriads of high-energy MS events were concentrated in these two zones, which also coincided with the results in Fig. 11(a). From the perspective of MS energy release, Zones II and III were more seriously damaged. A corresponding rock mass failure occurred in Zone II, as shown in Fig. 11(b). Indeed, a joint investigation of the distribution of MS events and radiated energy, excavation conditions and on-site observations can be performed to identify the excavation-induced damage regions and provide guidelines for the next steps in excavation and support.

3.5. *Formation mechanism and seismic characteristics of MS event clusters*

As mentioned above, an MS event refers to a localized rock mass failure. MS events are not random and are mainly clustered in specific regions where the rock masses are experiencing failure.[36] To better manage the failure risks of the surrounding rock mass and provide references for excavation and support, the formation mechanism and seismic characteristics of three MS event clusters in the underground powerhouse caverns are probed and analysed in this section.

3.5.1. *Formation mechanism of MS event clusters*

Generally, the MS event clusters in the underground powerhouse caverns are affected by different factors (e. g., excavation-

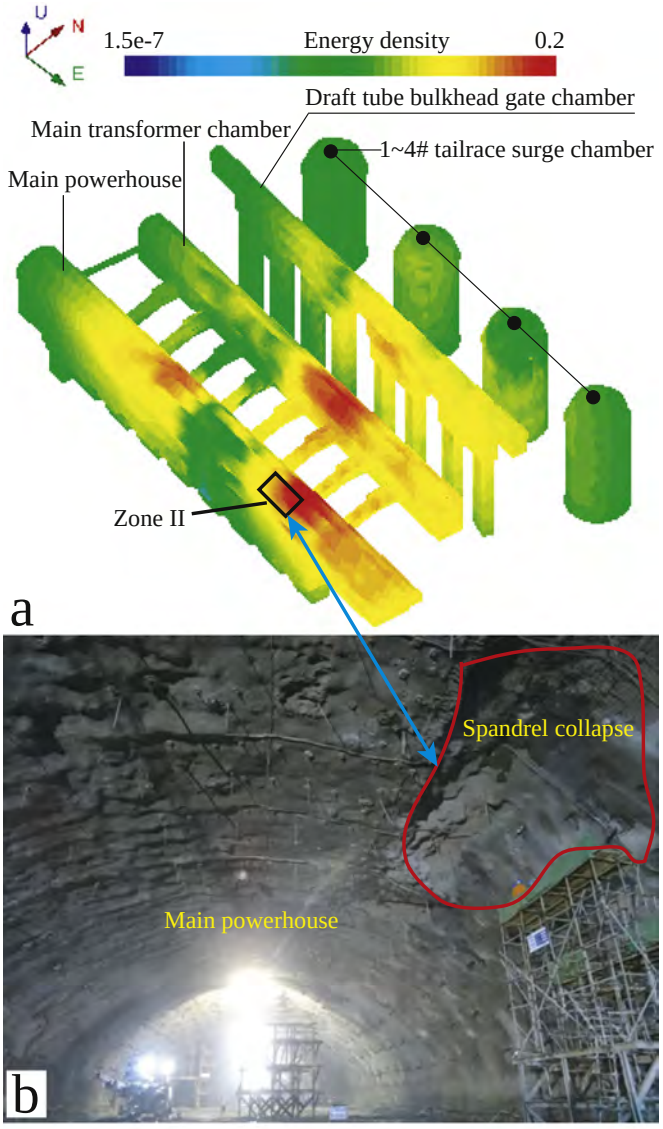

Fig. 11. (a) Contour of MS energy density, (b) rock collapse induced by high-energy MS events cluster (Zone II) in the main powerhouse.

induced unloading, geological structures, initial geo-stress, cavern sizes, cavern spatial arrangements). The MS event cluster is the visualization of the geo-stress and its evolution regularity.[14] Each of the three MS clusters in Fig. 10(b) was selected in a confined temporospatial range, as shown in Fig. 12(a), b and c. The MS cluster in zone I mainly occurred near the spandrel surface from October 15–21, 2014. The geological survey indicated that the rock mass in this region was relatively integrated, with no large geological structures exposed. However, from October 10–21, 2014, 21 blasts were recorded in the main powerhouse near zone I (see Fig. 12(a)). Therefore, the MS cluster in zone I was deduced to be mainly dominated by excavation-induced unloading, which occurred near the excavation surface within a short period. Fig. 12 (b) shows the MS cluster in zone II, with 196 MS events identified since the installation of the MS monitoring system. During the monitoring period, the MS events were consistently concentrated in this area. Combining the geological conditions, several discontinuities existed in zone II, such as fault f_{717}, long cracks T_{720}, T_{721} and internal staggered zones LS_{3254}, LS_{3152}, as illustrated in Fig. 12(b). Therefore, the aggregation of MS events around the geological structures indicated that the main effect for this MS cluster was excavation unloading-induced stress redistribution rather than direct excavation load. In zone III, 101 MS events were captured between October 14 and December 15, 2014. This MS cluster was aligned along the crown above unit 7 and unit 8 of the main powerhouse to the crown of the transformer chamber, clearly forming a stripped distribution, as shown in Fig. 12(c). This typical stripped distribution could be attributed to geological structure activation due to excavation. MS events might continue to concentrate in these geological structure areas as the lower benches of the caverns are excavated if no supporting measures are implemented.[32] The instability risk of the surrounding rock mass in the underground caverns would then increase.

3.5.2. *Seismic characteristics of MS event clusters*

Fig. 13 shows the magnitude-time histories of the three MS clusters in Fig. 12. The MS events are displayed with dates on the *x*-axis and moment magnitudes on the *y* axis. The moment magnitudes of the MS events in zone I range from −1.4 to 0.2. Nearly 90% of the MS events are in the moment magnitude range from −1.4 to −0.4, forming a normal distribution with a mean of −1.0. The moment magnitudes of the MS events in zone II range from −1.4 to 0.4, similarly following a normal distribution with a mean of −0.5. In zone III, the moment magnitudes of MS events are between −1.2 and 0.4. Meanwhile, the moment magnitudes similarly follow a normal distribution with a mean of −0.3. Relative to the events dominated by direct blasting (zone I), the MS events dominated by geological structures (zone II, III) have higher moment magnitudes, indicating more serious damage inside the surrounding rock mass.

Any seismic event emits a compression wave (P-wave) and a shear wave (S-wave). The energy of the P- and (S-wave)s can be calculated by the seismic monitoring system, and E_s/E_p is commonly used to analyse the seismic source mechanism.[15,36,37] Gibowicz et al.[37,38] stated that fault slip events typically produce much more energy in the (*s*-wave) than in the (*p*-wave). Boatwright and Fletcher[39] noted that an E_s/E_p in excess of 10 tends to reflect a fault slip mechanism, while a ratio closer to 3 indicates a non-shear mechanism. In addition, Gibowicz and Kijko[40] established a calculation formula, acquiring similar laws. According to these laws, a fault slip mechanism usually has an E_s/E_p value of more than 10. For non-shear events, such as stress-induced fracturing, tensile failure, and volumetric stress change events, the E_s/E_p was approximately 1–3. Cai et al.[24] developed a tensile model to estimate fracture size and found that 78% of 804 events had E_s/E_p less than 10 at the Underground Research Laboratory, which was in good agreement with the in situ tensile failure of the surrounding rock mass. This meaningful MS parameter was investigated in the underground powerhouse caverns. The E_s/E_p curves of MS events in zones I, II and III are shown in Fig. 14(a), b and c, respectively. In zone I, approximately 90% of MS events had an E_s/E_p below 10, which indicated that the dominant mechanism was non-shear associated with stress-induced fracturing from blasting excavation.[36] However, almost 55% and 60% of MS events exhibited an E_s/E_p of greater than 10 in zones II and III, respectively. Only approximately 15% and 20% of MS events in zones II and III, respectively, had an E_s/E_p value of less than 3. Thus, shear failure was dominant in the geological structure areas, such as zone II and III.

According to the formation mechanism and seismic parameters (i. e., moment magnitude and E_s/E_p) of the MS event clusters, different failure modes and characteristics of the surrounding rock mass were revealed. Depending on the excavation unloading, the mass spalling tended to occur near the free faces in zone I. Therefore, with regard to the MS event cluster in zone I, blasting rates should be controlled and shallow supports strengthened (e. g., anchoring and shotcreting, hanging steel bar mesh). With regard to zones II and III, deep instabilities (e. g., collapses,

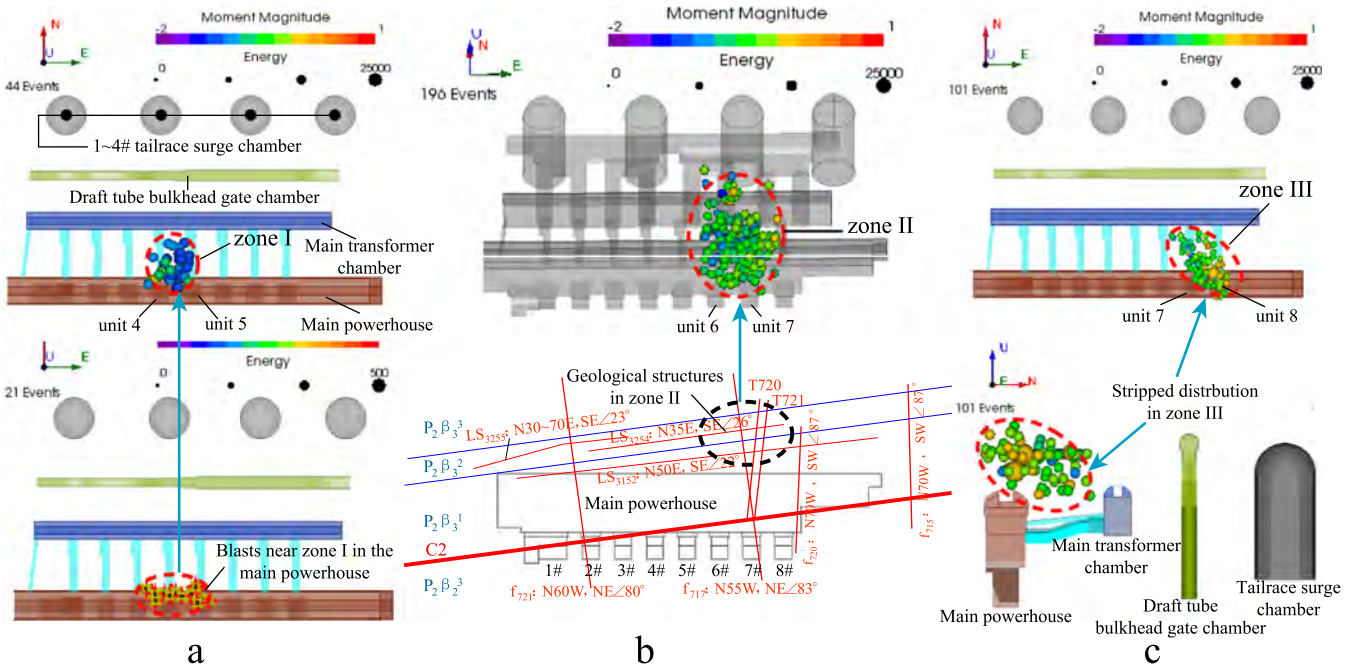

Fig. 12. MS event clustering mechanisms. (a) The MS event cluster dominated by excavation-induced unloading, (b) the MS event cluster dominated by geological structures, and (c) the stripped MS event cluster dominated by the activation of a geological structure.

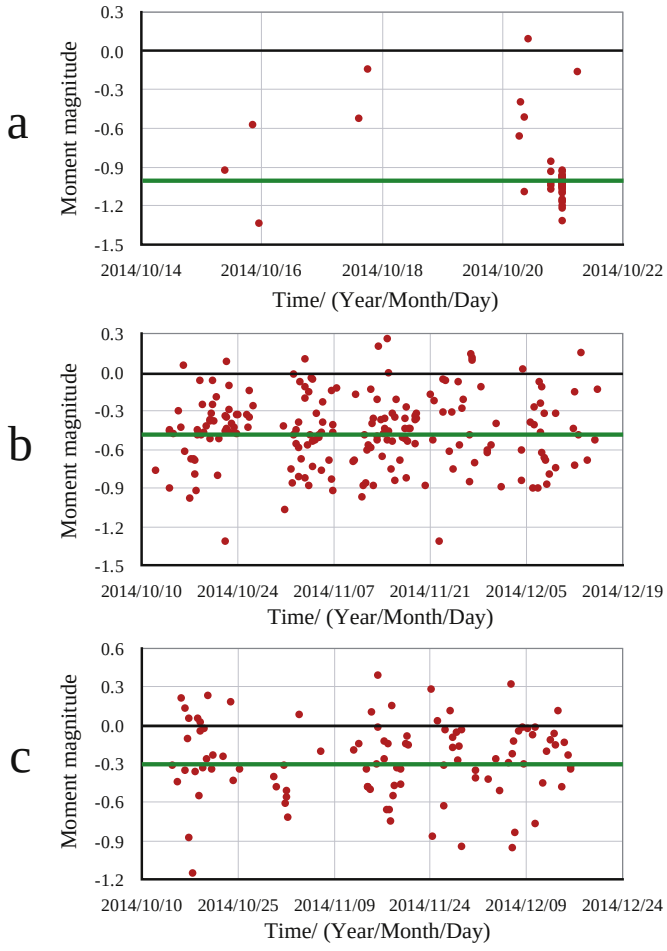

Fig. 13. Magnitude-time history charts of MS event clusters in zones (a) I, (b) II and (c) III. The blue lines represent the mean values of the similar normal distributions formed by the MS moment magnitudes of each MS cluster. (For interpretation of the references to color in this figure legend, the reader is referred to the web version of this article.)

rockbursts) dominated by geological structures were the main potential risks. In addition to reducing excavation near the MS cluster regions, cables and grouting supports should be implemented based on the geological information and evolutional characteristics of the MS events.

4. Deformation forecasting of surrounding rock mass based on MS data

For underground powerhouse caverns, most of the structures are permanent, and the deformation of the surrounding rock mass is quantitatively restricted. Therefore, deformation forecasting for the surrounding rock mass is of great significance for the construction of underground powerhouse caverns to guarantee field safety and guide the supports. In this section, an MS-based method is proposed to forecast the deformation of the surrounding rock mass.

4.1. Temporospatial evolution of MS events

Fig. 15(a) (red line) shows the temporal variation of MS events at the downstream spandrel between units 4 and 5 of the main powerhouse from October 10 to November 18, 2014. It can be observed that 33 MS events occurred in this region in October 20, 2014, far more than routine. Fig. 15(b) clearly illustrates the spatial aggregation and evolutional process of MS events. From October 10 to 18, 2014, only 9 MS events occurred in this region. However, a total of 48 MS events occurred in this studied area up to October 22, 2014, as 39 MS events were recorded from October 19–22, 2014. The MS activities then decreased, and 6 MS events were recorded between October 23 and 31, 2014. To further analyse the correlation between the MS monitoring and traditional monitoring methods, traditional monitoring data were collected from multipoint extensometers installed at the downstream spandrel aligned with unit 5 of the main powerhouse. Fig. 15(a) shows the location of the multipoint extensometer M_{ZC}-D-3 and its absolute displacement graph. The first bench excavation of the main powerhouse resulted in jumps in the displacement line between October 24, 2014, and November 16, 2014.

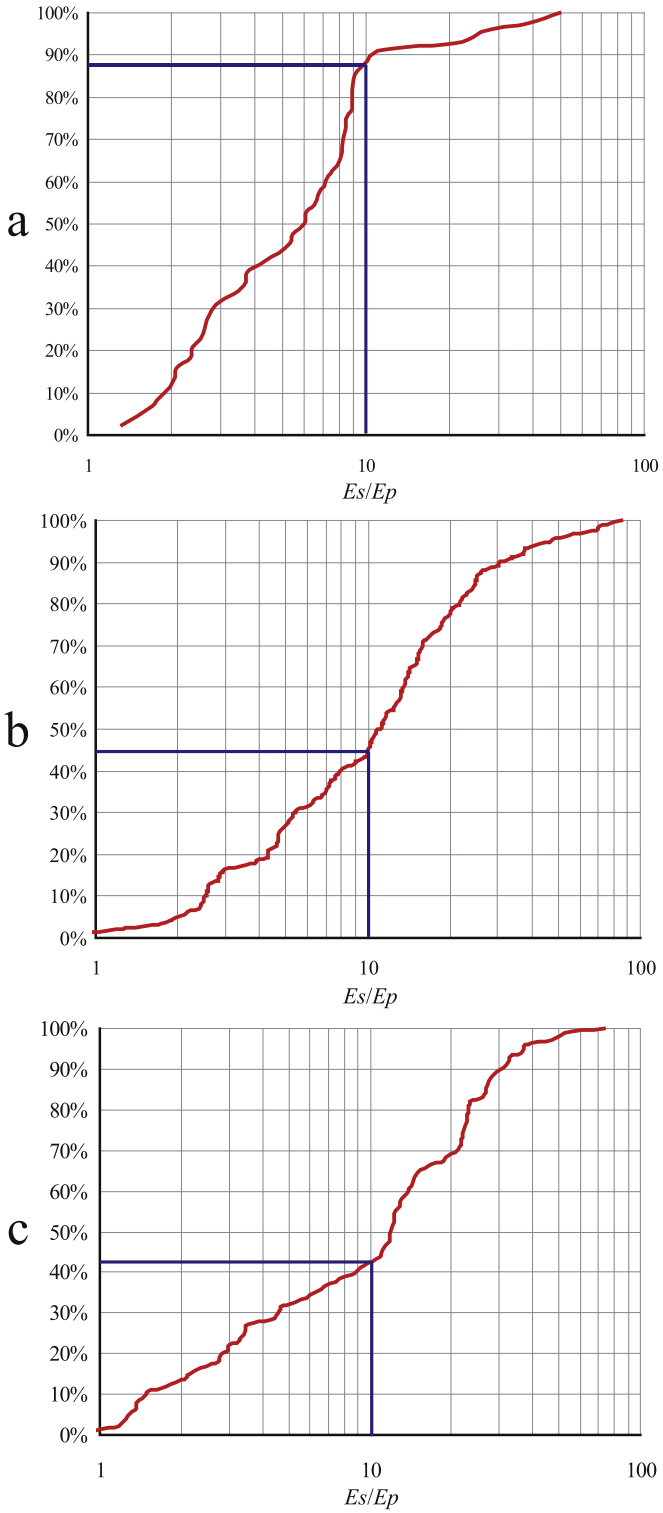

Fig. 14. E_s/E_p for MS clusters in zones (a) I, (b) II and (c) III.

During this period, more than 4 mm of deformation occurred at the downstream spandrel aligned with unit 5 of the main powerhouse. Coincidentally, the recorded MS events were concentrated near the downstream spandrel of the main powerhouse between unit 4 and 5, as shown in Fig. 15(b). An analysis of the supervised multipoint extensometer data indicated that the deformation of the downstream spandrel at the main powerhouse was closely related to the MS temporospatial evolution. However, the former results lagged behind the MS monitoring results. The aggregation of MS events at the downstream spandrel of the main powerhouse typically appeared 3–5 days before surface deformation of the surrounding rock mass was recorded in the multipoint extensometer M_{ZC}-D-3. Thus, the rapid propagation and accumulation of MS events in a localized area can be regarded as a precursor to the apparent deformation of the surrounding rock mass in the underground group caverns.

4.2. Laws of apparent stress and cumulative apparent volume

Statistical analyses of the temporospatial evolutional laws of MS events have been widely used to estimate underground rock mass stability.[21,41,42] From a seismological perspective, apparent stress and apparent volume are two significant parameters in describing the variation of the rock mass properties before and after the seismicity.

Unlike the estimation of source dimensions and stress drop, the determination of apparent stress in this study was largely independent of seismic models.[43–45] The apparent stress σ_A represents the level of stress release near a seismic source, defined as the radiated energy per unit volume of co-seismic inelastic deformation[46]:

$$\sigma_A = \frac{\mu E}{M_0} \tag{1}$$

The apparent volume V_A is defined as the volume of rock mass in the co-seismic inelastic deformation region[47]:

$$V_A = \frac{M_0}{2\sigma_A} = \frac{M_0^2}{2\mu E} \tag{2}$$

where μ is the shear modulus, M_0 is the seismic moment and E is the radiated energy. Both the apparent stress and the apparent volume depend on the seismic moment and radiated energy. Due to the scalar nature of σ_A and V_A, the calculated results can be manipulated in the form of diagrams and contours.

The regularities of apparent stress and cumulative apparent volume were selected for study during the deformation period of the surrounding rock mass. Fig. 16 shows the evolutional curve of the apparent stress and cumulative apparent volume of MS events from Fig. 15(b). The evolutional processes of these two parameters were divided into three stages (Stages a, b and c in Fig. 16). According to the process of the surrounding rock mass deformation in Fig. 15(a), Stage a (from October 10 to 18, 2014, in Fig. 16) and Stage b (from October 19 to 23, 2014, in Fig. 16) were the deformation smooth periods, while Stage 3 (from October 24 to November 16, 2014, in Fig. 16) was the deformation increase period. When the surrounding rock mass was in Stage a, the apparent stress was relatively small, and the cumulative apparent volume changed little, which can be regarded as a process of stress accumulation. In Stage b, the apparent stress increased sharply, and the cumulative apparent volume increased steadily. This stage can be regarded as the deformation forecasting period. Finally, in Stage c, the apparent stress decreased quickly, and the cumulative apparent volume increased steeply. Thus, a sharp increase in apparent stress associated with a steady increase in apparent volume can be regarded as another precursor to surrounding rock mass deformation in underground group caverns.

In summary, by analysing the tempo-spatial evolution of MS events and variations in apparent stress and cumulative apparent volume during the deformation period of surrounding rock mass in the Baihetan underground powerhouse caverns, a comprehensive deformation forecasting index can be proposed as follows: an abrupt increase and accumulation of MS events associated with a sharp increase in apparent stress and a steady increase in cumulative volume in the localized surrounding rock mass.

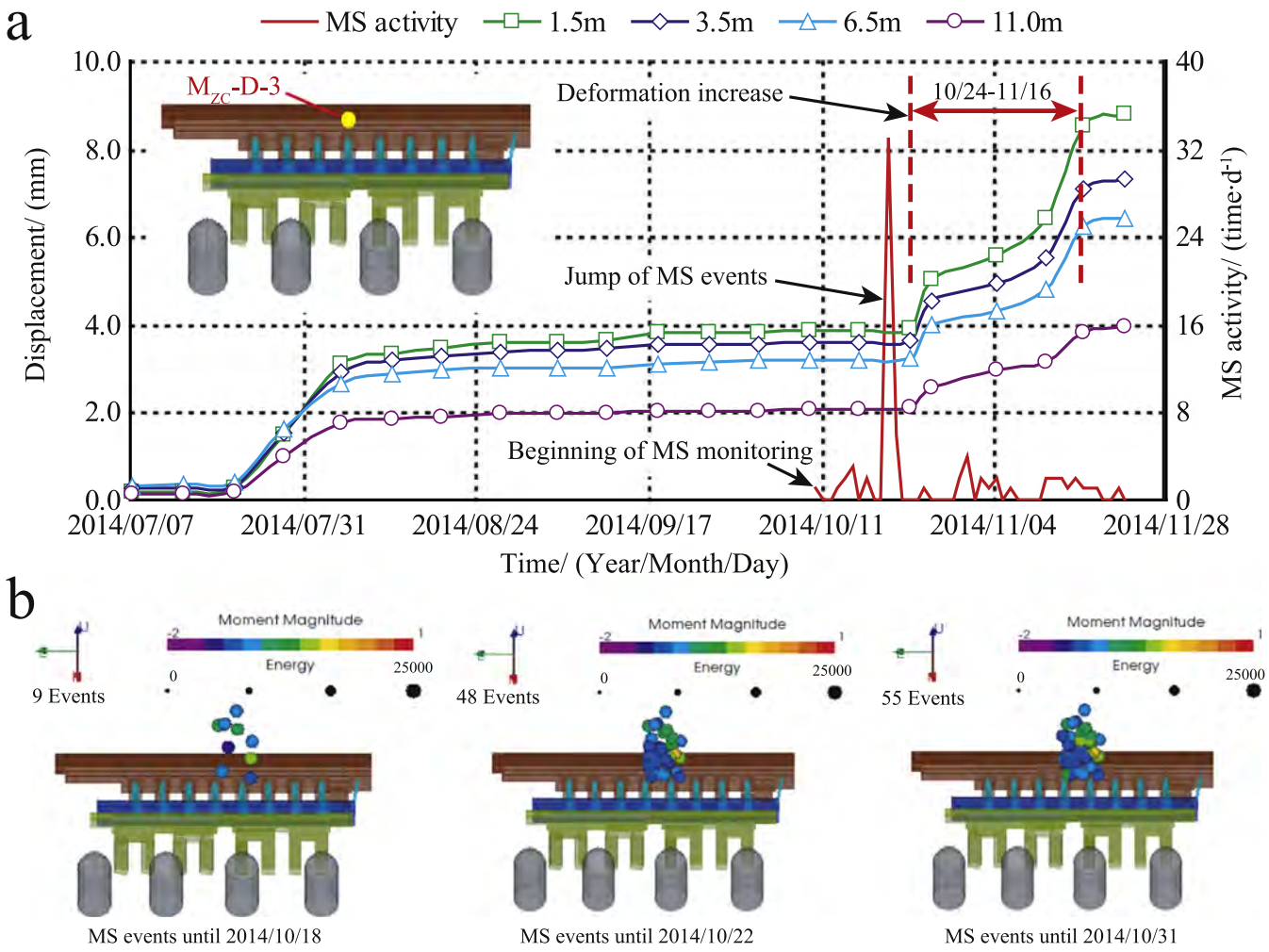

Fig. 15. Comparison between rock deformation and the temporospatial evolution of MS events. (a) Absolute displacement process of a multipoint extensometer M_{ZC}-D-3 and temporal evolution of MS events, and (b) spatial evolution of MS events. (For interpretation of the references to color in this figure, the reader is referred to the web version of this article.)

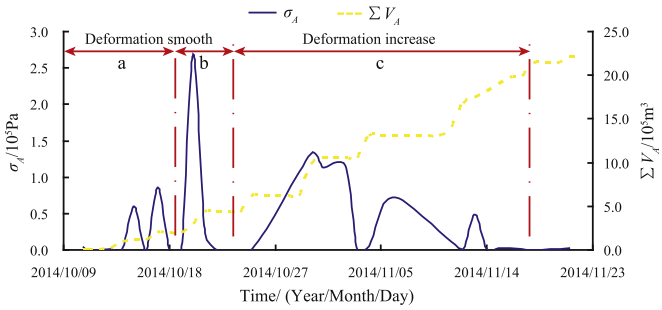

Fig. 16. Evolutions of apparent stress and cumulative apparent volume.

5. Conclusions

The MS monitoring technique was successfully used in the Baihetan underground powerhouse caverns for the real-time monitoring, analysis and estimation of the stability of the surrounding rock mass subjected to excavation. The temporal distribution of recorded MS events indicated that MS activity was sensitive to blasting excavation. Three main damage zones (Zone I, II and III in Fig. 10b) in the surrounding rock mass were identified based on the spatial distribution of MS events in the underground powerhouse caverns. In particular, in Zones II and III, where the seismic energy release was high, the surrounding rock was more severely damaged.

According to field construction and geological conditions, the mechanisms of the main MS clusters (see in Fig. 12a, b and c) were dominated by excavation-induced unloading and geological structure activations. For the MS cluster dominated by excavation-induced unloading, the moment magnitude was relatively low, and non-shear events dominated the rock mass failure mode. In contrast, the MS event clusters dominated by geological structure activations had higher moment magnitude, and the dominant failure was shear. Based on the characteristics of rock mass damage revealed by the formation mechanism and seismic parameters (i. e., moment magnitude and *Es*/*Ep*) of the MS event clusters, appropriate targeted supporting measures were suggested for the different damage zones.

A comprehensive deformation forecasting method for the surrounding rock mass was proposed based on the temporospatial evolution of MS events, apparent stress and cumulative apparent volume. The deformation forecasting index of the surrounding rock mass was summarized as an abrupt increase and accumulation of MS events accompanied by a sharp increase in apparent stress and a steady increase in cumulative volume in the localized surrounding rock mass. Therefore, the comprehensive analysis method, which incorporates MS monitoring, conventional monitoring, geological

survey and construction, is promising for identifying damage zones and forecasting the macro-deformation of the surrounding rock mass in underground powerhouse caverns subjected to excavation.

Acknowledgments

The authors are grateful for the financial support from the National Program on Key basic Research Project (No. 2015CB057903), National Natural Science Foundation of China (No. 51374149), Program for New Century Excellent Talents in University (NCET-13–0382) and the Youth Science and Technology Fund of Sichuan Province (2014JQ0004).

References

1. Zhu WS, Sui B, Li XJ, Li SC, Wang WT. A methodology for studying the high wall displacement of large scale underground cavern groups and it's applications. *Tunn Under Space Technol.* 2008;6:651–664.
2. Cai M, Kaiser PK, Morioka H, et al. FLAC/PFC coupled numerical simulation of AE in large-scale underground excavations. *Int J Rock Mech Min Sci.* 2007;44:550–564.
3. Alejanoa LR, RamõÂ rez-Oyanguren P, Taboada J. FDM predictive methodology for subsidence due to flat and inclined coal seam mining. *Int J Rock Mech Min Sci.* 1999;36(4):475–491.
4. Dhawan KR, Singh DN, Gupta ID. Three-dimensional finite element analysis of underground caverns. *Int J Geomech.* 2004;4:224–228.
5. Wang T, Chen XL, Yu LH. Discrete element calculation of surrounding rock mass stability of underground cavern group. *Rock Soil Mech.* 2005;26:1936–1940 [in Chinese].
6. Wu AQ, Ding XL, Chen SH, Shi GH. Researches on deformation and failure characteristics of an underground powerhouse with complicated geological conditions by DDA method. *Chin J Rock Mech Eng.* 2006;25:1–8 [in Chinese].
7. Jing L, Tsang CF, Stephansson O. DECOVALEX—an international co-operative research project on mathematical models of coupled THM processes for safety analysis of radioactive waste repositories. *Int J Rock Mech Min Sci.* 1995;32(5):389–398.
8. Zeng YW, Zhao ZY. Model testing studies of underground openings. *Chin J Rock Mech Eng.* 2001;20(suppl.1):1745–1749 [in Chinese].
9. Zhang ZX, Xu Y, Kulatilake PHSW, Huang X. Physical model test and numerical analysis on the behavior of stratified rock masses during underground excavation. *Int J Rock Mech Min Sci.* 2012;49:134–147.
10. Li SJ, Yu H, Liu YX, Wu FJ. Results from in-situ monitoring of displacement, bolt load, and disturbed zone of a powerhouse cavern during excavation process. *Int J Rock Mech Min Sci.* 2008;45:1519–1525.
11. Hibino S, Motojima M. Anisotropic behavior of jointed rock mass around large-scale caverns. In: *Proceedings of the 9th International Congress on Rock Mech.* Sandton, Paris; 1999. 385–388.
12. Yan P, Lu WB, Chen M, Hu YG, Zhou CB, Wu XX. Contributions of in-situ stress transient redistribution to blasting excavation damage zone of deep tunnels. *Rock Mech Rock Eng.* 2014, http://dx.doi.org/10.1007/s00603–014–0571–3.
13. Lynch RA, Wuite R, Smith BS, Cichowicz A. Micro-seismic monitoring of open pit slopes. In Micro-seismic monitoring of open pit slopes. In: Potvin Y, Hudyma M, eds. *Proceedings of the 6th Symposium on Rockbursts and Seismicity in Mines.* Perth, Australia: ACG; 2005:581–92.
14. Xu NW, Tang CA, Li LC, et al. Microseismic monitoring and stability analysis of the left bank slope in Jinping first stage hydropower station in southwestern China. *Int J Rock Mech Min Sci.* 2011;48:950–963.
15. Xu NW, Dai F, Liang ZZ, Zhou Z, Sha C, Tang CA. The dynamic evaluation of rock slope stability considering the effects of microseismic damage. *Rock Mech Rock Eng.* 2014;47:621–642.
16. Young RP, Collins DS, Reyes-Montes JM, Baker C. Quantification and interpretation of seismicity. *Int J Rock Mech Min Sci.* 2004;41:1317–1327.
17. Ge MC. Efficient mine microseismic monitoring. *Int J Coal Geol.* 2005;64:44–56.
18. Lesniak A, Isakow Z. Space-time clustering of seismic events and hazard assessment in the Zabrze-Bielszowice coal mine, Poland. *Int J Rock Mech Min Sci.* 2009;46:918–928.
19. Trifu CI, Shumila V. Microseismic monitoring of a controlled collapse in Field II at Ocnele Mari, Romania. *Pure Appl Geophys.* 2010;167:27–42.
20. Tang LZ, Wang LH, Zhang J, Li XB. Seismic apparent stress and deformation in a deep mine under large-scale mining and areal hazardous seismic prediction. *Chin J Rock Mech Eng.* 2011;30(6):1168–1178 [in Chinese].
21. Liu JP, Feng XT, Li YH, Xu SD, Sheng Y. Studies on temporal and spatial variation of microseismic activities in a deep metal mine. *Int J Rock Mech Min Sci.* 2013;60:171–179.
22. Wang CL. Identification of early-warning key point for rockmass instability using acoustic emission/microseismic activity monitoring. *Int J Rock Mech Min Sci.* 2014;71:171–175.
23. Li SL. Discussion on microseismic monitoring technology and its application to underground project. *Chin J Under Space Eng.* 2009;5(1):122–128 [in Chinese].
24. Cai M, Kaiser PK, Martin CD. A tensile model for the interpretation of microseismic events near underground openings. *Pure Appl Geophys.* 1998;153:67–92.
25. Cai M, Kaiser PK, Martin CD. Quantification of rock mass damage in underground excavations from microseismic event monitoring. *Int J Rock Mech Min Sci.* 2001;38:1135–1145.
26. Tang CA, Wang JM, Zhang JJ. Preliminary engineering application of microseismic monitoring technique to rockburst prediction in tunneling of Jinping II project. *J Rock Mech Geotech Eng.* 2011;2(3):193–208.
27. Feng XT, Chen BR, Li SJ, et al. Studies on the evolution process of rockbursts in deep tunnels. *J Rock Mech Geotech Eng.* 2012;4(4):289–295.
28. Chen BR, Feng XT, Li QP, Luo RZ, Li SJ. Rock burst intensity classification based on the radiated energy with damage intensity at Jinping II hydropower station, China. *Rock Mech Rock Eng.* 2015;48(1):289–303.
29. Tezuka K, Niitsuma H. Stress estimated using microseismic clusters and its relationship to the fracture system of the Hijiori hot dry rock reservoir. *Eng Geol.* 2000;56:47–62.
30. HydroChina Huadong Engineering Corporation. Bidding Documents Reference of Civil Engineering and Installation of Metal Structures of the Left Bank Water Diversion and Power Generation System in Baihetan Hydropower Station; 2013:21–44. [in Chinese].
31. Cai M, Morioka H, Kaiser PK, et al. Back-analysis of rock mass strength parameters using AE monitoring data. *Int J Rock Mech Min Sci.* 2007;44(4):538–549.
32. Xu NW, Li TB, Dai F, Li B, Zhu YG, Yang DS. Microseismic monitoring and stability evaluation for the large scale underground caverns at the Houziyan hydropower station in Southwest China. *Eng Geol.* 2015;188:48–67.
33. Xu NW, Tang CA, Li H, Wu SH. Optimal design of micro-seismic monitoring array and seismic source location estimation for rock slope. *Open Civ Eng J.* 2011;5:36–45.
34. Martino JB, Chandler NA. Excavation-induced damage studies at the underground research laboratory. *Int J Rock Mech Min Sci.* 2004;41(8):1413–1426.
35. Li B, Dai F, Xu NW, et al. Microseismic monitoring system establishment and its engineering applications to deep-buried underground powerhouse. *Chin J Rock Mech Eng.* 2014;33(Suppl.1):3375–3384 [in Chinese].
36. Hudyma M, Potvin YH. An engineering approach to seismic risk management in hardrock mines. *Rock Mech Rock Eng.* 2010;43:891–906.
37. Gibowicz SJ, Young RP, Talebi S, Rawlence DJ. Source parameters of seismic events at the Underground Research Laboratory in Manitoba, Canada: scaling relations for events with moment magnitude smaller than −2. *Bull Seism Soc Am.* 1991;81:1157–1182.
38. Urbancic TI, Young RP, Bird S, Bawden W. Microseismic source parameters and their use in characterizing rock massbehaviour: considerations from Strathcona mine. In: *Proceedings of 94th annual general meeting of the CIM: Rock Mechanics and Strata Control Sessions*, Montreal, 26–30 April 1992; 1992:36–47.
39. Boatwright J, Fletcher JB. The partition of radiated energy between P and S waves. *Bull Seism Soc Am.* 1984;74(2):361–376.
40. Gibowicz SJ, Kijko A. *An Introduction to Mining Seismology.* 1st ed., San Diego: Academic Press.; 1994:396.
41. Zhang PH, Yang TH, Yu QL, et al. Microseismicity induced by fault activation during the fracture process of a crown pillar. *Rock Mech Rock Eng.* 2014, http://dx.doi.org/10.1007/s00603–014–0659–9.
42. Lu CP, Liu GJ, Liu Y, Zhang N, Xue JH, Zhang L. Microseismic multi-parameter characteristics of rockburst hazard induced by hard roof fall and high stress concentration. *Int J Rock Mech Min Sci.* 2015;76:18–32.
43. Trifu CI, Urbancic TI, Young RP. Source parameters of mining-induced seismic event: an evaluation of homogeneous and inhomogeneous faulting model for assessing damage potential. *Pure Appl Geophys.* 1995;145(1):3–27.
44. Snoke JA, Linde AT, Sacks IS. Apparent stress: an estimate of the stress drop. *Bull Seism Soc Am.* 1983;73(2):339–348.
45. Gibowicz SJ, Harjes HP, Schäfer M. Source parameters of seismic events at Heinrich Robert mine, Ruhr Basin, Federal Republic of Germany: evidence for nondouble-couple events. *Bull Seism Soc Am.* 1990;80(1):88–109.
46. Wyss M, Brune JN. Seismic moment, stress and source dimensions for earthquakes in the California-Nevada region. *J Geophys Res.* 1968;73(14):4681–4694.
47. Mendecki AJ. Real time quantitative seismology in mines. In: *Proceedings of Sixth International Symposium on Rockburst and Seismicity in Mines.* Rotterdam: A. A. Balkema; 1993:287–295.